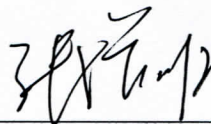




	指导教师姓名	张增明	职称	教授
指导教师评语	对学生发表论文评语及论文情况说明：			
	<p>宋文申同学是 2010 级中国科学技术大学少年班学院的本科生，他的研究课题源自于大学物理-研究性实验。该同学积极主动、实验动手能力强、善于抓住实验细节，对实验现象有自己独立的见解。在前期研究性实验的基础上，他提出开展极端条件下的材料的结构与光学性质研究，设计利用物理手段来调控荧光材料的结构、吸收、能量转移等，进而调谐材料光学性能。能自己提出物理模型和方法，解释材料温压-结构-发光性能之间构效关系，具有创新性。</p> <p>指导教师（签名）： 2016年5月31日</p>			
学校推荐意见	<p>宋文申是 2010 级中国科学技术大学少年班学院的本科生。他在张增明教授指导下开展了极端条件下 $\text{YBO}_3:\text{Eu}/\text{Tb}$ 荧光材料的结构与光学性质课题研究，相关成果已在高水平的国际期刊发表，受到国外专家的好评与认可，该研究成果已被引用多次。经学院讨论，一致同意推荐宋文申同学参加此次全国实验研讨会的学生论文评比。</p> <p>负责人（签名）： 公章  2016年5月31日</p>			
	<p>大会学术组专家意见</p> <p>专家组组长（签名）：_____ 年 月 日</p>			
评比结果	<p>大会主席（签名）_____ 年 月 日</p>			

PAPER

CrossMark
click for updatesCite this: *J. Mater. Chem. C*, 2015, 3, 2405Received 14th September 2014
Accepted 10th January 2015

DOI: 10.1039/c4tc02061h

www.rsc.org/MaterialsCRaman scattering and photoluminescence investigation of $\text{YBO}_3:\text{Eu}^{3+}$ under high temperature and high pressure†W. S. Song,^a G. X. Y. Huang,^a R. C. Dai,^{*b} Z. P. Wang^b and Z. M. Zhang^{*b}

Raman scattering, X-ray diffraction and photoluminescence spectra of $\text{YBO}_3:\text{Eu}^{3+}$ are measured at high temperatures up to 1323 K. Results show that a temperature-induced phase transition from the LT to the HT phase starts at about 1273 K, then the HT phase transforms into the LT phase on cooling to 873 K. A theoretical model based on a luminescent dynamic process describes the temperature-dependent emission intensity well. In this model, the contributions from thermal activation, phonon-assisted absorption, and nonradiative energy transfer are analyzed in detail. In addition, we report the structure and optical behavior of $\text{YBO}_3:\text{Eu}^{3+}$ under high pressure by means of Raman scattering and photoluminescence measurements. When pressure is increased from zero to 25 GPa, Raman and photoluminescence measurements show that the structure of $\text{YBO}_3:\text{Eu}^{3+}$ remains stable and no pressure-driven phase transition occurs throughout the entire pressure range of these experiments. In addition, the mode-Grüneisen parameters and thermal expansion coefficient are calculated.

Introduction

$\text{YBO}_3:\text{Eu}^{3+}$ is widely used in plasma display panels, Hg-free fluorescent lamps and light-emitting diodes due to its high vacuum ultraviolet transparency, excellent luminescence efficiency, and strong chemical and structural stability.^{1–5} Up to now, as far as quantum efficiency and vacuum ultraviolet absorption are concerned, $\text{YBO}_3:\text{Eu}^{3+}$ is still one of the best red phosphors. However, the characteristic emission of ${}^5\text{D}_0 \rightarrow {}^7\text{F}_1$ is almost equal to the transition ${}^5\text{D}_0 \rightarrow {}^7\text{F}_2$, which gives rise to an orange-red emission and relatively poor color chromaticity. Nevertheless, the ${}^5\text{D}_0 \rightarrow {}^7\text{F}_2$ transition is hypersensitive to the symmetry of the local crystal field surrounding Eu^{3+} ions and that transition would be relatively strong if the crystal field symmetry is low. Therefore, several attempts have been made to solve the chromaticity drawback of $\text{YBO}_3:\text{Eu}^{3+}$ by means of reducing the symmetry of the crystal field.

Many investigators are devoted to enhancing the ${}^5\text{D}_0 \rightarrow {}^7\text{F}_2$ emission using various chemical means, such as controlling the morphology and size of $\text{YBO}_3:\text{Eu}^{3+}$. Wei *et al.* synthesized sphere-like $\text{YBO}_3:\text{Eu}^{3+}$ nanoparticles and found that the red and orange (R/O) intensity ratio is much higher in the smaller sized particles.⁴ They thought that distorted crystal lattices should be

responsible for this superior chromaticity. Zhang *et al.* reported the hierarchical architecture of $\text{YBO}_3:\text{Eu}^{3+}$ with nano- and micro-structures and considered that the improvement in color chromaticity was attributed to distinct multilayers in the samples.⁶ Besides, the luminescence intensity of $\text{YBO}_3:\text{Eu}^{3+}$ can also be enhanced by co-dopants Bi^{3+} , Li^+ and alkaline-earth metal ions,^{7,8} which play important roles in tuning the energy transfer process, particle size and surface morphology.

A well-defined crystal structure of the compounds is crucial to improve their fluorescence performance and luminescence properties. YBO_3 exists in two types of phase structures: low-temperature (LT) phase and high-temperature (HT) phase. The LT phase is a monoclinic cell with $C2/c$ space group, in which B_3O_9 rings are the only borate species under ambient conditions, whereas the HT phase crystallizes in a monoclinic cell with all isolated plane BO_3 groups under the $C2/c$ space symmetry.⁹ Gu *et al.* investigated the structure of YBO_3 at various temperatures, using *in situ* Raman spectroscopy and observed a reversible structural transition from the LT phase to the HT phase.¹⁰ A high-pressure X-ray diffraction study of $\text{YBO}_3:\text{Eu}^{3+}$ was performed by Wang *et al.* and they found that $\text{YBO}_3:\text{Eu}^{3+}$ is stable up to 41 GPa;¹¹ the bulk moduli of $\text{YBO}_3:\text{Eu}^{3+}$ was refined to be 141 GPa by Errandonea *et al.*¹²

Despite the advances mentioned above, the present understanding of the structure and optical properties of $\text{YBO}_3:\text{Eu}^{3+}$ is not sufficient, especially for high temperature and high pressure. It is well known that Eu^{3+} ions are sensitive to their local environment, thus the presence and splitting of the selected Eu^{3+} electronic transitions could be an excellent probe for structural studies. In this article, the temperature- and pressure-

^aSchool of the Gifted Young, University of Science and Technology of China, Hefei, Anhui 230026, China

^bThe Centre of Physical Experiments, University of Science and Technology of China, Hefei, Anhui 230026, China. E-mail: zzm@ustc.edu.cn; dairc@ustc.edu.cn

† Electronic supplementary information (ESI) available. See DOI: 10.1039/c4tc02061h

dependent structure and optical behavior of $\text{YBO}_3:\text{Eu}^{3+}$ are investigated in detail using the Raman scattering method and a luminescence probe technique for Eu^{3+} .

Experimental

Sample preparation

$\text{YBO}_3:\text{Eu}^{3+}$ was prepared by a solid-state reaction. 4.5 mmol Y_2O_3 (99.99% purity), 0.5 mmol Eu_2O_3 (99.99% purity) and 10.25 mmol H_3BO_3 (99.99% purity) were mixed (H_3BO_3 is 2.5 mol% excess on account of the volatility of B_2O_3). At first, the mixture was ground for 1 h and then heated to 773 K for 2 h to decompose the boric acid. After cooling to room temperature, the mixture was ground for 1 h and heated again to 1373 K for 2 h.

Characterization

X-ray diffraction (XRD) was carried out on a X-ray diffractometer (Rigaku, TTR III) under $\text{Cu K}\alpha$ radiation. Particle size and morphology was characterized by a field emission scanning electron microscope (FE-SEM, SU8010). Emission and excitation spectra were collected by a steady-state/lifetime spectrofluorimeter (JOBIN YVON, FLUOROLOG-3-TAU) equipped with a 450 W xenon lamp as the excitation source. PL and Raman spectra were collected by an integrated laser Raman system (LABRAMHR, Jobin Yvon) with a confocal microscope, a stigmatic spectrometer, and a multichannel air cooled charge coupled device (CCD) detector. High temperature measurements were carried out by flowing high purity nitrogen into a TS 1500 furnace (Linkam, England). The sample was heated to the desired temperature using 50 K increments for each step and held for 10 min before collecting Raman spectra under ambient pressure. We used an excitation wavelength of 514.5 nm at 1323 K, and 785 nm at other temperatures to prevent the effects of fluorescence to the largest extent. High pressure was generated by using a diamond anvil cell (DAC) technique with a stainless steel gasket. The 200 μm gasket was preindented and then a hole, with a diameter of 170 μm , was made in its center using a spark drill. Silicon oil was used as the pressure transmitting medium. A few grains of ruby powder were applied for *in situ* pressure measurements by the standard ruby fluorescence technique.¹³ The pressure was calibrated by the shift of the ruby R_1 fluorescence line.

Results and discussion

Characterization of $\text{YBO}_3:\text{Eu}^{3+}$

Fig. 1 shows SEM images of the as-prepared $\text{YBO}_3:\text{Eu}^{3+}$ sample and after annealing at 1573 K. The as-synthesized sample shows agglomeration of small particles with diameters from 100 to 500 nm. After annealing at 1573 K, the particles grow and coagulate and the boundaries between particles become hard to identify. Fig. 2 displays the XRD pattern of the $\text{YBO}_3:\text{Eu}^{3+}$ sample at room temperature. All the diffraction peaks of these samples can be matched well to ICDD card no. 04-014-2922, and the crystal structure is indexed to a pure LT phase YBO_3 , crystallizing in a monoclinic pseudowollastonite-type structure with $C2/c$ space

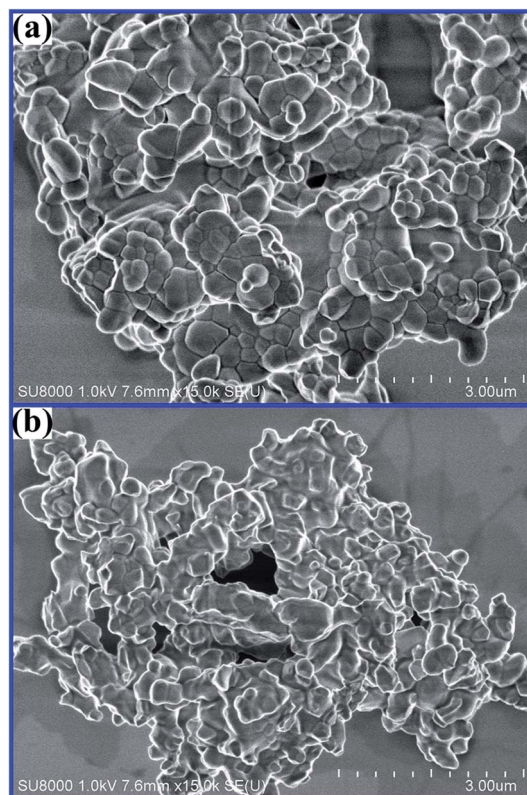


Fig. 1 SEM images of $\text{YBO}_3:\text{Eu}^{3+}$ samples; (a) as-prepared powder, (b) heat-treated at 1573 K.

group.^{9,14,15} No additional peak of another phase has been found, which also indicates that the existence of Eu^{3+} does not cause significant change to the host structure and the obtained samples are in a single phase.

The excitation spectra of $\text{YBO}_3:\text{Eu}^{3+}$ with emission wavelengths of 621.5 nm and 610.5 nm are given in Fig. 3 at ambient conditions. The intense edge from 250 nm to 270 nm corresponds to the charge transfer (CT) between O^{2-} and Eu^{3+} . The characteristic absorption peaks of Eu^{3+} ions can be observed in

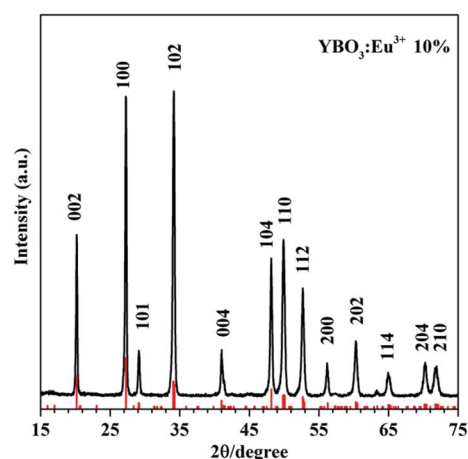


Fig. 2 X-ray diffraction pattern of $\text{YBO}_3:\text{Eu}^{3+}$ sample.

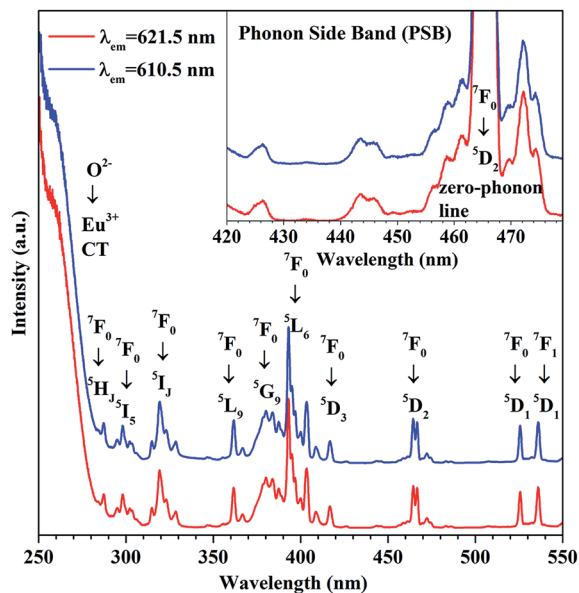


Fig. 3 Excitation and phonon side band (PSB) spectra of the $\text{YBO}_3:\text{Eu}^{3+}$ sample at ambient conditions.

the range 280–550 nm (assigned in Fig. 3). These peaks correspond to the direct excitation of europium f-electrons from the ground state to higher excited states.⁷ The inset of Fig. 3 shows the phonon side band (PSB), in which the zero phonon line is at 465 nm and the one phonon line is around 445 nm for the ${}^7\text{F}_0 \rightarrow {}^5\text{D}_2$ transition. Therefore, the Huang–Rys factor (S) can be calculated as follows:¹⁶

$$S = I_{1p}/I_{zp} \quad (1)$$

where I_{1p} and I_{zp} are the intensities of the one phonon line and the zero phonon line, respectively. The S value is 0.080. This factor is an important constant for constructing the luminescent dynamic equation.

The emission spectra of $\text{YBO}_3:\text{Eu}^{3+}$ at ambient conditions with an excitation wavelength of 514.5 nm are shown in Fig. 4. Normally, Eu^{3+} generates luminescence due to the transitions from the excited ${}^5\text{D}_0$ level to ${}^7\text{F}_J$ ($J = 0, 1, 2, 3, 4$) levels of the $4f^6$ configuration. The Eu^{3+} characteristic emission peaks at around 581 nm are from the ${}^5\text{D}_0 \rightarrow {}^7\text{F}_0$ transition; the peaks in the range 585–595 nm originate from the ${}^5\text{D}_0 \rightarrow {}^7\text{F}_1$ transition; the peaks in the range 600 to 640 nm are assigned to the ${}^5\text{D}_0 \rightarrow {}^7\text{F}_2$ transition; several peaks in the range 640–660 nm are due to the ${}^5\text{D}_0 \rightarrow {}^7\text{F}_3$ transition. The number of splits is closely interrelated with specific local sites occupied by the Eu^{3+} ions. As for $\text{YBO}_3:\text{Eu}^{3+}$ with $C2/c$ space group, the Eu^{3+} ion mainly occupies the C_1 and C_i sites of the Y^{3+} ion.¹⁷ For C_1 , the number of bands for each ${}^5\text{D}_0 \rightarrow {}^7\text{F}_J$ ($J = 0, 1, 2, 3, 4$) transition is 1, 3, 5, 7 and 9, respectively; for C_i , the numbers correspond to 0, 3, 0, 0 and 0. Thus, the number of bands in the PL spectra should be 1 for ${}^5\text{D}_0 \rightarrow {}^7\text{F}_0$, 6 for ${}^5\text{D}_0 \rightarrow {}^7\text{F}_1$, 5 for ${}^5\text{D}_0 \rightarrow {}^7\text{F}_2$, and 7 for ${}^5\text{D}_0 \rightarrow {}^7\text{F}_3$ (other splits are not taken into consideration). The emission spectra can be decomposed to several Lorentz lineshape peaks, which are all in accordance with the theoretical splitting

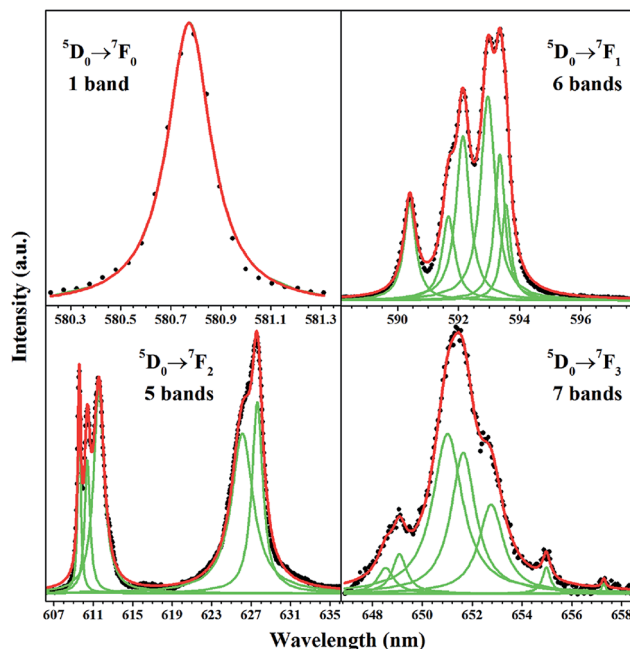


Fig. 4 PL spectra with Lorentz fitting of the $\text{YBO}_3:\text{Eu}^{3+}$ sample at ambient conditions.

number as seen in Fig. 4. This consistency confirms the site symmetry of Y^{3+} and space group of $\text{YBO}_3:\text{Eu}^{3+}$. Combined with the excitation spectra, the energy level values of Eu^{3+} are listed in Table 1.

The Raman spectrum for $\text{YBO}_3:\text{Eu}^{3+}$ at ambient conditions is shown at the bottom of Fig. 5. The LT phase $\text{YBO}_3:\text{Eu}^{3+}$ exhibits vibrational bands typical for B_3O_9 rings. The B_3O_9 ring has D_{3h} symmetry with twelve atoms, which leads to 20 vibrational modes represented as:¹⁰

$$\Gamma = 4A'_1 + A''_1 + 2A'_2 + 3A''_2 + 6E' + 4E''$$

Among which $4A'_1 + 6E' + 4E''$ are Raman active. The B–O–B bending of the BO_4 units includes Raman bands at 260 cm^{-1} , 295 cm^{-1} , 358 cm^{-1} , 378 cm^{-1} , 413 cm^{-1} , 432 cm^{-1} , 490 cm^{-1} and 508 cm^{-1} . B_3O_9 borate ring deformation includes Raman bands at 614 cm^{-1} , 669 cm^{-1} , 723 cm^{-1} and 837 cm^{-1} . The 1003 cm^{-1} and 1035 cm^{-1} bands can be assigned to the

Table 1 Energy levels and deviations of Eu^{3+} in $\text{YBO}_3:\text{Eu}^{3+}$ (units, cm^{-1})

${}^7\text{F}_0$	${}^7\text{F}_1$	${}^7\text{F}_2$	${}^7\text{F}_3$	${}^5\text{D}_0$	${}^5\text{D}_1$	${}^5\text{D}_2$
0.0	280.8	814.0	1798.9	17 218.4	19 025.9	21 533.2
	317.1	836.0	1812.0			21 431.6
	330.6	867.3	1857.8			
	353.8	1247.0	1872.6			
	365.0	1285.7	1898.9			
	370.7		1950.7			
			2004.3			

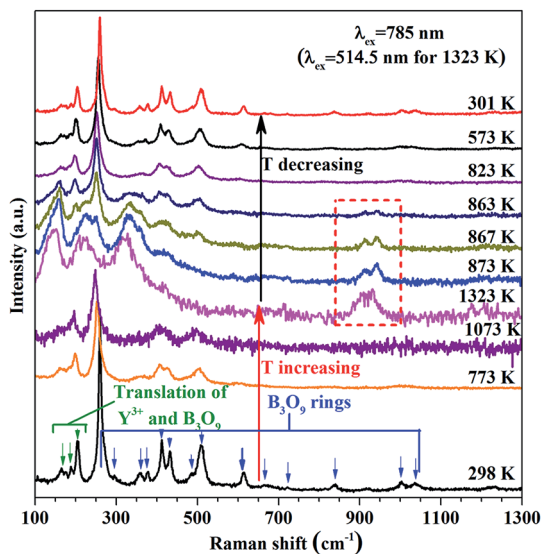


Fig. 5 Raman scattering of $\text{YBO}_3:\text{Eu}^{3+}$ within the temperature range of 298–1323 K (excited by 785 nm laser under 1323 K and 514.5 nm laser at 1323 K).

stretching of tetrahedral BO_4 groups, which share vertices, thus forming three-membered ring borate B_3O_9 units. Raman modes under 250 cm^{-1} , such as 166 cm^{-1} , 189 cm^{-1} and 205 cm^{-1} are attributed to the translation of the Y^{3+} cations and the B_3O_9 groups.¹⁸ All these Raman peaks provide evidence for the existence of B_3O_9 rings in the LT phase.

Temperature-dependent Raman, XRD and PL spectra

Fig. 5 shows the Raman spectra for $\text{YBO}_3:\text{Eu}^{3+}$ at different temperatures under ambient pressure. With increasing temperature, Raman peaks shift to low-frequency and their corresponding intensities decrease. This is due to the increase of temperature-induced interatomic distances and widening of the bond angle distribution, causing distortions of the crystal structure.¹⁹ When the temperature reaches 1323 K, some new Raman peaks appear more obvious, corresponding to isolated BO_3 triangles. The point group symmetry of the isolated BO_3 group is D_{3h} , which leads to vibrational modes represented as:¹⁰ $\Gamma = A'_1 + A'_2 + 2E'$. Characteristic Raman peaks of BO_3 units, observed at around 940 cm^{-1} , are assigned to the symmetric stretching mode $A'_1(\nu_1)$, which splits into two Raman peaks because the occupation site of the BO_3 group is less than threefold symmetry in the HT phase. In addition, the peak at around 1200 cm^{-1} , is assigned to the asymmetric stretching mode $E'(\nu_3)$. The Raman bands between 620 cm^{-1} and 800 cm^{-1} are assigned to out-plane bending mode $A''_2(\nu_2)$. These bands prove the existence of the BO_3 group in the HT phase YBO_3 .¹⁰ Moreover, vibrational modes at 159 cm^{-1} , 226 cm^{-1} and 331 cm^{-1} could be the translation of the Y^{3+} cations and the BO_3 units. It can be concluded that during the heating process, the B–O bonds of the BO_4 groups break apart and isolated BO_3 plane conjugated groups are formed. As presented in ESI Fig. S1a,[†] temperature-dependent XRD confirms that the LT

phase transformation into the HT phase in $\text{YBO}_3:\text{Eu}^{3+}$ starts at 1273 K. During the cooling process, Raman spectra reveal the HT phase of $\text{YBO}_3:\text{Eu}^{3+}$ transforms into the LT phase at 873 K, which is consistent with observations in the XRD patterns of $\text{YBO}_3:\text{Eu}^{3+}$ as shown in ESI Fig. S1b.[†] There is a large thermal hysteresis existing between these two phase transitions. The reason is that the phase transformation of YBO_3 has a higher apparent activation energy for heating process, forming a large potential barrier.²⁰

Fig. 6 shows the PL emission spectra of $\text{YBO}_3:\text{Eu}^{3+}$ from 294 to 1323 K with an excitation wavelength of 514.5 nm. With increasing temperature, the $^5\text{D}_0 \rightarrow ^7\text{F}_0$ transition exhibits only one emission band, and the emission peak linearly shifts towards a shorter wavelength. For the $^5\text{D}_0 \rightarrow ^7\text{F}_1$ transition, at 294 K, six obvious peaks can be distinguished in the region of 590–595 nm (also seen in Fig. 4); when the temperature reaches 523 K, two new peaks appear at 583 and 585 nm, similar to those seen in the PL spectra of Eu^{3+} in Y_3BO_6 .²¹ As discussed above, the two site occupations C_i and C_1 in $\text{YBO}_3:\text{Eu}^{3+}$ can only lead to a single peak for $^5\text{D}_0 \rightarrow ^7\text{F}_0$. Y_3BO_6 has various types of symmetry sites, which would bring about a complicated splitting of energy levels, especially distinct multi-peaks for $^5\text{D}_0 \rightarrow ^7\text{F}_0$, as described elsewhere.¹⁷ However, because only one peak can be observed for $^5\text{D}_0 \rightarrow ^7\text{F}_0$, and the XRD pattern also indicates a pure phase for YBO_3 , there is no sign of Y_3BO_6 phase existence. Therefore, it is possible that 10 mol% doping of Eu^{3+} brings in some new local symmetry similar to that in Y_3BO_6 , without changing the phase purity. The new splits for the $^5\text{D}_0 \rightarrow ^7\text{F}_0$ transition caused by this doping effect are too weak to detect at room temperature, but when the temperature increases, these new peaks become stronger. The six peaks merge into three peaks in the range 590–595 nm and two new peaks are

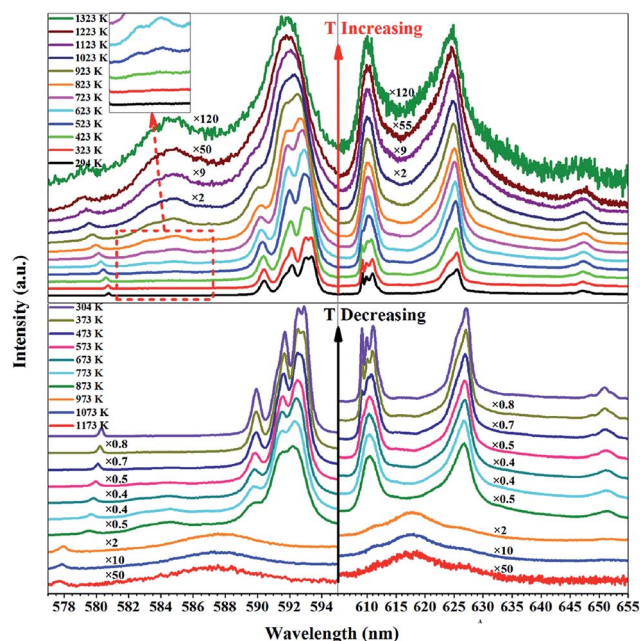


Fig. 6 PL spectra of $\text{YBO}_3:\text{Eu}^{3+}$ with an excitation wavelength of 514.5 nm during the heating and cooling processes.

maintained for the ${}^5D_0 \rightarrow {}^7F_1$ transition from 623 to 1323 K. As for the ${}^5D_0 \rightarrow {}^7F_2$ transition, it has three emission peaks located within the range of 605–615 nm, and two peaks within the range 620–635 nm at 294 K. With the increase of temperature, the former three emission peaks gradually merge into one peak and the latter two peaks broaden into one peak. The results show that the position of the ${}^5D_0 \rightarrow {}^7F_2$ transition move very little with increasing temperature. As for the ${}^5D_0 \rightarrow {}^7F_3$ transition, the peaks do not shift but become wider with increasing temperature. The phase transitions in the heating process are hardly noticeable from the PL spectra, due to the indistinguishable emissions of the $\text{YBO}_3:\text{Eu}^{3+}$ HT phase in a strong thermal radiation background at 1373 K. As presented in ESI Fig. S2,† the R/O value increases monotonically with increasing temperature, indicating that temperature can effectively improve the color chromaticity of $\text{YBO}_3:\text{Eu}^{3+}$. During the cooling process, PL spectra gradually become distinguishable at 1173 K. New emission peaks at 578, 587 and 617 nm appear while the original peaks disappear, indicating a big change of local site symmetry. This is an indication of phase transition and characteristic emissions of the HT-phase $\text{YBO}_3:\text{Eu}^{3+}$ are clearly observed. When the temperature decreases to 873 K, the PL spectra gradually become similar to those of the starting materials, indicating the transformation of the HT phase into the LT phase. On cooling, an abrupt leap in R/O is found at 873 K as shown in ESI Fig. S2,† suggesting the HT phase transforms into the LT phase at this temperature.

The decay curves for the $\text{YBO}_3:\text{Eu}^{3+}$ monitored at 593 nm for Eu^{3+} emission are measured from 298 K to 673 K and are displayed in Fig. 7. All the decay curves can be reasonably fitted *via* a single-exponential function. It is obvious that increasing temperature from 298 K to 673 K leads to slightly shortening the lifetime of Eu^{3+} (that is, from 3.16 ms to 2.81 ms). In this case, the energy transfer between Eu^{3+} ions and non-radiative decay at defects are more likely to take place, thus resulting in a shorter lifetime.

Fig. 8 shows temperature-dependent total emission intensity of the ${}^5D_0 \rightarrow {}^7F_J$ ($J = 0, 1, 2, 3$) transitions at an excitation wavelength of 514.5 nm. With increasing temperature, the maximum intensity can be seen at about 900 K. The process can

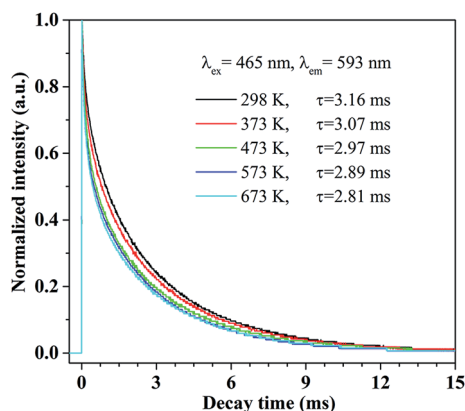


Fig. 7 Temperature dependence decay curves of Eu^{3+} emission detected at 593 nm for the $\text{YBO}_3:\text{Eu}^{3+}$ sample.

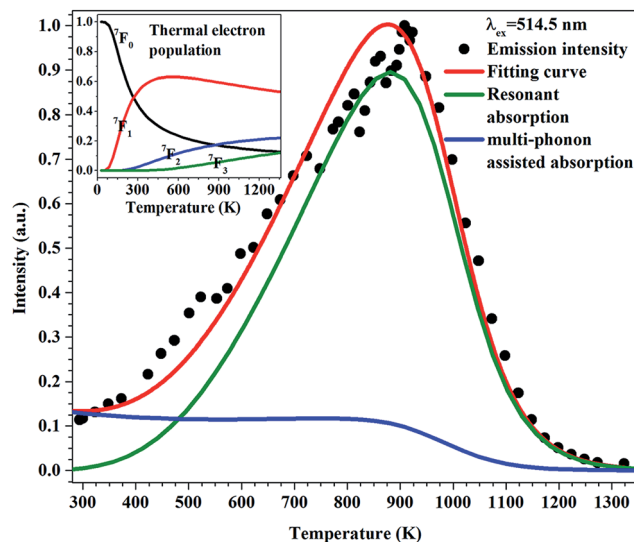


Fig. 8 Normalized total emission intensity of ${}^5D_0 \rightarrow {}^7F_{0,1,2,3}$ as a function of temperature. The dots are experimental data and the solid lines are fitting functions. The inset is the population of ${}^7F_{0,1,2,3}$ levels as a function of temperature.

be explicated by a model based on a luminescence dynamic equation, considering thermal activation, phonon-assisted absorption, and a nonradiative energy transfer process.²² For $\text{YBO}_3:\text{Eu}^{3+}$, whose splitting energy levels have already been determined previously, the total emission intensity of $\sum_J {}^5D_0 \rightarrow {}^7F_J$ ($J = 0, 1, 2, 3$) can be written as:

$$I(T) \propto \frac{\sum N_i(T) \sigma_i(T)}{1 + W_T(T)/\gamma_0} \quad (2)$$

where I is the pumping light power density, W_T is the temperature-quenching rate, γ_0 is the radiative transition rate and $\sigma_i(T)$ is the absorption cross section. $N_i(T) = \frac{e^{-\Delta E_i/kT}}{\sum_i e^{-\Delta E_i/kT}}$ gives

the thermal electron population on different splitting levels in 7F_J ; i represents each splitting energy level, ΔE_i is the energy separation from these levels to 7F_0 and k is the Boltzmann constant. Moreover, multi-phonon absorption, resonant absorbing processes, and the temperature-quenching rate are taken into account, and the fitting formula can be written as

$$I(T) = \frac{\beta_1 \left[\sum_{ij} e^{-\alpha E_{ij}} \times (1 + \langle n \rangle)^{E_{ij}/\hbar\omega} + \sum_{i,k} e^{-\alpha E_{ik}} \times \langle n \rangle^{E_{ik}/\hbar\omega} \right] e^{-\Delta E_i/kT}}{\sum_i e^{-\Delta E_i/kT} \times (1 + \beta_3 e^{T/T_c})} + \frac{\beta_2 e^{-\Delta E_i/kT}}{\sum_i e^{-\Delta E_i/kT} \times (1 + \beta_3 e^{T/T_c})} \quad (3)$$

in which $\beta_1 = I\sigma_1$, $\beta_2 = I\sigma_2$, and $\beta_3 = W_T(0)/\gamma_0$. The right side of eqn (3) includes two terms. The first mainly illustrates multi-phonon absorption processes. For non-resonant excitation, the electrons can reach ${}^5D_{0,1,2}$ levels with the assistance of phonons (higher 5D_J states are not taken into consideration because the

transition probability is too small to accumulate enough electrons). In the numerator, the summation terms, including subscripts i, j and i, k , represent the absorbing and emitting phonon process, respectively. $E_{i,j}$ and $E_{i,k}$ are the energy differences between the energy of a 514.5 nm photon and the energy separation from the target transition levels. The first term, $\alpha = \frac{1}{\hbar\omega} [\ln(E_{i,j(k)}/\hbar\omega) - 1 - \ln S]$, where S is the Huang–Rhys factor, provides a quantitative description of electron-phonon coupling. $n = \frac{1}{e^{\hbar\omega/kT} - 1}$ is the phonon density. As for the second term, the resonant absorption process is demonstrated. In consideration of the 7F_3 splitting Stark levels, the excitation at 514.5 nm can be in resonance with the ${}^7F_3 \rightarrow {}^5D_2$ transition. Note that other possible transitions from the higher 7F_j states are neglected due to the very low thermal electron populations compared to ${}^7F_{1,2,3}$. Besides, the $\frac{1}{1 + \beta_3 e^{T/T_c}}$ item coexisting in both terms arises from the temperature-quenching effect. Energy levels of Eu^{3+} in $\text{YBO}_3:\text{Eu}^{3+}$ are given in Table 1. Other constants are listed below: Huang–Rhys factor $S = 0.080$, calculated from phonon side band (PSB) spectra; Boltzmann constant $k = 0.6948 \text{ cm}^{-1} \text{ K}^{-1}$; $\hbar\omega = 1035 \text{ cm}^{-1}$, obtained from Raman spectra.

As seen in Fig. 8, the emission intensity with varying temperature can be reasonably well fitted and the fitting parameters are determined as: $\beta_1 = 0.22$, $\beta_2 = 164.19$, $\beta_3 = 5.05 \times 10^{-8}$, $T_c = 58.11$. The contribution of the multi-phonon assisted absorption and resonant absorption processes are displayed. The emission intensity, derived from the multi-phonon assisted absorption process, exhibits an overall declining trend with increasing temperature; whereas the resonant absorption process, which plays a dominant role in luminescence, has a maximum emission intensity around 900 K. Thus, the emission intensity with varying temperature can be ascribed to two main factors. The inset in Fig. 8 shows the thermal electron population with varying temperature. The population number 7F_3 level increases with temperature. This indicates that the first dominating factor is the excitation from 7F_3 to 5D_2 , which can make the emission intensity increase monotonically within the temperature range of 294–1323 K. The second factor is the temperature-quenching effect, causing the emission intensity to decrease with temperature. The theoretical model and fitting results help to improve our understanding of the luminescence dynamic process of $\text{YBO}_3:\text{Eu}^{3+}$.

Pressure-dependent PL and Raman spectra

Fig. 9 shows the PL emission spectra of $\text{YBO}_3:\text{Eu}^{3+}$ under high pressure up to 25 GPa. With increasing pressure, the ${}^5D_0 \rightarrow {}^7F_{0,1}$ transitions shift almost linearly to longer wavelengths and broaden, meanwhile their emission intensities decrease. The red-shift is due to the fact that the pressure strengthens the interaction between Eu^{3+} and O^{2-} ions, thus energy levels for 5D_0 and ${}^7F_{0,1}$ will get close and the energy level difference decreases. For the ${}^5D_0 \rightarrow {}^7F_2$ transition, the four obvious peaks between 605 and 620 nm gradually merge into one and the right peak slightly blue-shifts with pressure. For the band from 625 to

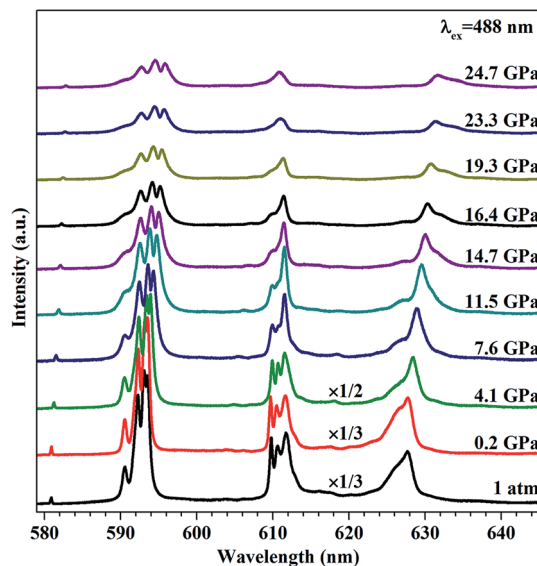


Fig. 9 PL spectra of $\text{YBO}_3:\text{Eu}^{3+}$ with an excitation wavelength of 488 nm during compression.

630 nm, there is an obvious red-shift with a comparatively high rate. With increasing pressure, the left peak gradually diminishes while a new peak in the right appears slowly around 14.7 GPa. This could be caused by a pressure-induced change of site symmetry. The reason why two groups of ${}^5D_0 \rightarrow {}^7F_2$ peaks move to opposite directions is that the electric dipole driving the ${}^5D_0 \rightarrow {}^7F_2$ transition from 608 to 634 nm is easily affected by the crystal field. The increase of pressure results in smaller distances and stronger interaction between atoms, thus strengthening the crystal field around Eu^{3+} . This aggravates the splitting of 7F_2 , and the two groups of peaks gradually separate, causing the blue-shift of high-energy peaks and the red-shift of low-energy peaks. Moreover, the ratio of R/O decreases with the increase of pressure as seen in ESI Fig. S3,† indicating that the site symmetry rises and the covalency of the Eu–O bond weakens. Because no apparent discontinuity can be observed in ESI Fig. S3,† we can deduce that no phase transitions occurred on increasing pressure. When the pressure is released, the PL spectrum recovers to its original state, suggesting a good stability of $\text{YBO}_3:\text{Eu}^{3+}$ under high pressure up to 25 GPa.

Fig. 10 displays the evolution of Raman modes of $\text{YBO}_3:\text{Eu}^{3+}$ with increasing pressure. This shows a shift to high frequency and broadening of Raman peaks without any change in line shape. The intensities of these peaks diminish quickly with pressure and most peaks cannot be identified above 10 GPa due to the pressure-induced broadening effect. Still, several characteristic modes of B_2O_3 can be identified and their frequencies increase to high wavenumber at different rates. The reason is that the pressure reduces the distance between atoms, leading to the increase of vibrational energy. From the Raman spectra, several interesting physical parameters can be obtained, including pressure coefficients, which reflect the shifting rates of Raman modes; the Grüneisen parameter γ , which plays a crucial role in understanding the thermodynamic and thermoelastic behavior of solids; as well as the molar heat capacity

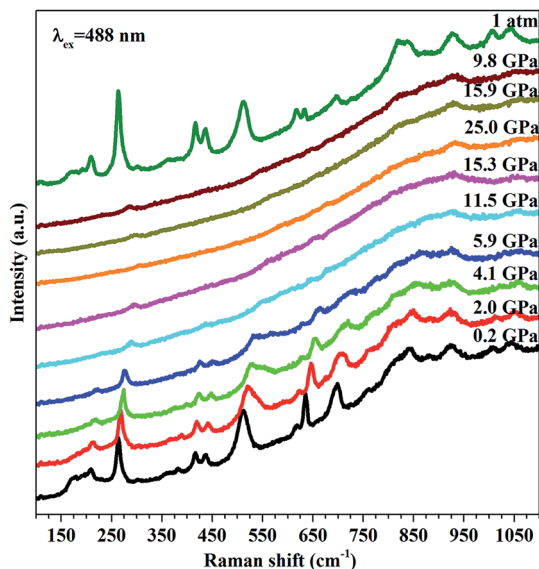


Fig. 10 Raman scattering of $\text{YBO}_3:\text{Eu}^{3+}$ with an excitation wavelength of 488 nm during compression and decompression.

and thermal expansion coefficient.²³ By linear fitting, pressure coefficients $d\omega/dP$ are calculated from Raman spectra. The mode Grüneisen parameter γ_i can be calculated by:^{24,25}

$$\gamma_i = - \left(\frac{\partial \ln \omega_i}{\partial \ln V} \right) = \frac{B}{\omega_{0i}} \left(\frac{d\omega_i}{dP} \right) \quad (4)$$

where ω_{0i} is the frequency of the vibrational mode and B is the bulk modulus whose value is 141 GPa.¹² The molar heat capacity of a single mode can be expressed as:²³

$$C_i = R \frac{(E_i/k_B T)^2 e^{E_i/k_B T}}{(e^{E_i/k_B T} - 1)^2} \quad (5)$$

where $E_i = \hbar\nu_i$ is the energy of a single vibrational mode, while k_B is the Boltzmann constant and R is the ideal gas constant. The values of Raman modes at ambient pressure ω_i , the pressure coefficient $d\omega_i/dP$, the mode Grüneisen parameter γ_i and

Table 2 Raman active modes at ambient pressure with their pressure coefficients, as well as Grüneisen parameter γ and molar heat capacity for each mode

ω (cm^{-1})	$d\omega/dP$ ($\text{cm}^{-1} \text{GPa}^{-1}$)	γ	C_i ($\text{J mol}^{-1} \text{K}^{-1}$)
209.9	1.56	1.05	7.65
264.5	1.89	1.01	7.28
301.2	1.99	0.93	7.01
363.2	1.68	0.65	6.50
382.5	3.23	1.19	6.33
416.7	1.92	0.65	6.02
436.7	2.77	0.89	5.84
513.8	3.1	0.85	5.13
618.7	2.64	0.60	4.18
838.5	3.98	0.67	2.50
1005	5.35	0.75	1.58
1038	5.98	0.81	1.44

single mode molar heat capacity C_i are listed in Table 2. With that, we can calculate the total heat capacity at constant volume $C_v = \sum C_i = 61.44$ and the average Grüneisen parameter $\gamma_{av} = \sum C_i \gamma_i / C_v = 0.87$. Because γ_{av} can be also expressed as $\gamma_{av} = 3\alpha V_m B_0 / C_v$, and molar unit-cell volume at ambient pressure V_m is $6.56 \times 10^{-5} \text{ m}^3 \text{ mol}^{-1}$, we can obtain the linear thermal expansion coefficient α as $1.93 \times 10^{-6} \text{ K}^{-1}$. Because the Grüneisen parameter γ and thermal expansion coefficient α of $\text{YBO}_3:\text{Eu}^{3+}$ are not reported so far, the values of γ and α in our calculation gives a necessary understanding of the thermo-elastic behavior of $\text{YBO}_3:\text{Eu}^{3+}$. On the release of pressure, Raman peaks gradually recover to their starting state, indicating that the structure of $\text{YBO}_3:\text{Eu}^{3+}$ is fairly stable up to 25 GPa.

Conclusions

At ambient pressure, Raman scattering and XRD show that a reversible phase transition from the LT phase to the HT phase takes place at about 1273 K. From the PL spectra, the local sites of Eu^{3+} in YBO_3 crystal are well interpreted to be C_1 and C_i based on the splitting of $^5D_0 \rightarrow ^7F_{0,1,2,3}$ transitions. This corroborates the $C2/c$ space group of YBO_3 , in accordance with the neutron diffraction study of Lin *et al.*⁹ After the heating-induced phase transition, the characteristic emissions of the HT-phase $\text{YBO}_3:\text{Eu}^{3+}$ are clearly observed on cooling to 1173 K, and then turn into those of the LT-phase at 873 K. This observation of phase transition is consistent with the results given by Raman scattering and XRD. The R/O ratio of Eu^{3+} ion increases with increasing temperature, and an abrupt leap in the R/O ratio is found on decreasing temperature to 873 K. Besides, the temperature-dependent emission intensity can be reasonably well calculated by a theoretical model based on the luminescence dynamic equations. As for ambient temperature, Raman scattering reveals that the structure of $\text{YBO}_3:\text{Eu}^{3+}$ remains stable at a pressure of 25 GPa. The Grüneisen parameter γ and thermal expansion coefficient α of $\text{YBO}_3:\text{Eu}^{3+}$ are 0.87 and $1.93 \times 10^{-6} \text{ K}^{-1}$, respectively. The emissions of $\text{YBO}_3:\text{Eu}^{3+}$ shift to longer wavelengths and the R/O ratio reduces with increasing pressure indicating a lower asymmetry around the Eu^{3+} ions while no phase transition takes place on compression. Therefore, the luminescence of Eu^{3+} ions can serve as an excellent probe for structural studies of materials.

Acknowledgements

This work was supported by the National Natural Science Foundation of China (no. 11304300), the National Basic Research Program of China (no. 2011CB932801 and 2012CB933702), the Fundamental Research Funds for the Central Universities (Grant no. WK2030420002) and Anhui Provincial Natural Science Foundation (1308085QA06).

Notes and references

- 1 W. Chen and A. Zhou, *J. Phys. Chem. C*, 2012, **116**, 24748–24751.

- 2 V. Jubera, J. P. Chaminade, A. Garcia, F. Guillen and C. Fouassier, *J. Lumin.*, 2003, **101**, 1–10.
- 3 Z. Li, J. Zeng and Y. Li, *Small*, 2007, **3**, 438–443.
- 4 Z. Wei, L. Sun, C. Liao, J. Yin, X. Jiang, C. Yan and S. Lü, *J. Phys. Chem. B*, 2002, **106**, 10610–10617.
- 5 X.-C. Jiang, C.-H. Yan, L.-D. Sun, Z.-G. Wei and C.-S. Liao, *J. Solid State Chem.*, 2003, **175**, 245–251.
- 6 X. Zhang, A. Marathe, S. Sohal, M. Holtz, M. Davis, L. J. Hope-Weeks and J. Chaudhuri, *J. Mater. Chem.*, 2012, **22**, 6485–6490.
- 7 L. Chen, G. Yang, J. Liu, X. Shu, G. Zhang and Y. Jiang, *J. Appl. Phys.*, 2009, **105**, 013513.
- 8 D. Jin, J. Yang, X. Miao, L. Wang, S. Guo, N. Wang and L. Wang, *Mater. Lett.*, 2012, **79**, 225–228.
- 9 J. Lin, D. Sheptyakov, Y. Wang and P. Allenspach, *Chem. Mater.*, 2004, **16**, 2418–2424.
- 10 G. X. Gu, D. Wang, X. S. Lv, S. M. Wan, J. L. You, Q. L. Zhang and S. T. Yin, *Mater. Chem. Phys.*, 2011, **131**, 274–277.
- 11 P. Wang, D. He, C. Xu, X. Ren, L. Lei, S. Wang, F. Peng, X. Yan, D. Liu, Q. Wang, L. Xiong and J. Liu, *J. Appl. Phys.*, 2014, **115**, 043507.
- 12 D. Errandonea, A. Muñoz and J. Gonzalez-Platas, *J. Appl. Phys.*, 2014, **115**, 216101.
- 13 H. K. Mao, P. M. Bell, J. W. Shaner and D. J. Steinberg, *J. Appl. Phys.*, 1978, **49**, 3276–3283.
- 14 P. Morgan, P. Carroll and F. Lange, *Mater. Res. Bull.*, 1977, **12**, 251–259.
- 15 A. Pitscheider, R. Kaindl, O. Oeckler and H. Huppertz, *J. Solid State Chem.*, 2011, **184**, 149–153.
- 16 Y. Tian, X. Qi, X. Wu, R. Hua and B. Chen, *J. Phys. Chem. C*, 2009, **113**, 10767–10772.
- 17 G. Jia, P. A. Tanner, C.-K. Duan and J. Dexpert-Ghys, *J. Phys. Chem. C*, 2010, **114**, 2769–2775.
- 18 Y. Wu, D. Ding, F. Yang, S. Pan and G. Ren, *Mater. Res. Bull.*, 2012, **47**, 106–110.
- 19 G. E. Walrafen, S. R. Samanta and P. N. Krishnan, *J. Chem. Phys.*, 1980, **72**, 113–120.
- 20 J. Plewa and T. Jüstel, *J. Therm. Anal. Calorim.*, 2007, **88**, 531–535.
- 21 D. Boyer, G. Bertrand-Chadeyron, R. Mahiou, A. Brioude and J. Mugnier, *Opt. Mater.*, 2003, **24**, 35–41.
- 22 J. Wang, H. Song, X. Kong, W. Xu and H. Xia, *J. Appl. Phys.*, 2002, **91**, 9466–9470.
- 23 J. Ruiz-Fuertes, D. Errandonea, O. Gomis, A. Friedrich and F. J. Manjón, *J. Appl. Phys.*, 2014, **115**, 043510.
- 24 R. C. Dai, L. B. Luo, Z. M. Zhang and Z. J. Ding, *Mater. Res. Bull.*, 2011, **46**, 350–354.
- 25 M. R. Joya, J. Barba-Ortega and P. S. Pizani, *J. Appl. Phys.*, 2013, **113**, 013512.